Crystal–Glass High-Entropy Nanocomposites with Near Theoretical Compressive Strength and Large Deformability

Ge Wu, Shanoob Balachandran, Baptiste Gault, Wenzhen Xia, Chang Liu, Ziyuan Rao, Ye Wei, Shaofei Liu, Jian Lu, Michael Herbig, Wenjun Lu,* Gerhard Dehm, Zhiming Li,* and Dierk Raabe*

High-entropy alloys (HEAs) and metallic glasses (MGs) are two material classes based on the massive mixing of multiple-principal elements. HEAs are single or multiphase crystalline solid solutions with high ductility. MGs with amorphous structure have superior strength but usually poor ductility. Here, the stacking fault energy in the high-entropy nanotwinned crystalline phase and the glass-forming-ability in the MG phase of the same material are controlled, realizing a novel nanocomposite with near theoretical yield strength ($G/24$, where G is the shear modulus of a material) and homogeneous plastic strain above 45% in compression. The mutually compatible flow behavior of the MG phase and the dislocation flux in the crystals enable homogeneous plastic co-deformation of the two regions. This crystal–glass high-entropy nanocomposite design concept provides a new approach to developing advanced materials with an outstanding combination of strength and ductility.

Dr. G. Wu, Dr. S. Balachandran, Dr. B. Gault, Dr. W. Xia, Dr. C. Liu, Z. Rao, Y. Wei, Dr. M. Herbig, Dr. W. Lu, Prof. G. Dehm, Prof. Z. Li, Prof. D. Raabe
Max-Planck-Institut für Eisenforschung
Max-Planck-Straße 1, Düsseldorf 40237, Germany
E-mail: w.lu@mpie.de; d.raabe@mpie.de

Dr. B. Gault
Department of Materials
Royal School of Mines
Imperial College
Prince Consort Road, London SW7 2BP, UK

S. Liu, Prof. J. Lu
Department of Mechanical Engineering
City University of Hong Kong
Hong Kong, China

Prof. Z. Li
School of Materials Science and Engineering
Central South University
Changsha 410083, China
E-mail: lizhiming@csu.edu.cn

Prof. Z. Li
State Key Laboratory of Powder Metallurgy
Central South University
Changsha 410083, China

The ORCID identification number(s) for the author(s) of this article can be found under https://doi.org/10.1002/adma.202002619.

Strategies widely employed for strengthening crystalline alloys typically involve introducing crystalline imperfections such as secondary phases and associated interphases, grain or twin boundaries, and foreign atoms in solid solution. These strengthening mechanisms are mainly based on controlling the generation and propagation of dislocations, the typical carriers of plasticity. Among these approaches, coherent nanoscale precipitation[1] and transformation induced plasticity[2] have been shown to enable improvements in both strength and ductility also in the recently developed high-entropy alloys (HEAs) containing multiple principal elements. HEAs, introduced in the last decade,[3] are single- or multiphase crystalline solid solutions with a wide spectrum of mechanical properties.[4] Their crystalline solid solution nature usually enables high ductility, carried by dislocation slip, twinning, or phase transformation.[1,2,4,5] Furthermore, by controlling composition and microstructure, the strength of the HEAs can be significantly enhanced, in some cases even exceeding that of conventional crystalline alloys.[6] Yet, the shear strength of HEAs does not exceed $G/100$, and thus is far from the theoretical limit of approximately $G/10$.[7] Metallic glasses (MGs), introduced in the 1960s,[8] do not possess slip systems and lattice dislocations,[9] manifest superior yield shear strength of $G/37$.[9,10] However, the plastic deformation of MGs at ambient temperature is highly localized in shear bands,[9] thus leading to MGs' catastrophic failure without any significant macroscopic ductility. Introducing structural heterogeneity, that is, liquid-like regions or, respectively, soft zones, into the MG matrix[11] is a design technique that is capable of deflecting and deferring the propagation of shear bands during deformation, thus enhancing ductility.[12] Another exception occurs when MGs undergo homogeneous plastic flow in cases where their size is reduced below 100 nm.[13,14] Based on that and the recent advance in the development of HEAs,[1,2,4] we present a novel material design concept combining amorphous MG and crystalline HEA phases at the nanoscale to realize a novel material class with superior mechanical properties. This is achieved by creating crystal–glass high-entropy nanocomposites, realized here by doping glass-forming elements into a high-entropy Cr–Fe–Co–Ni system, which allows to access compositional regimes where

**ADVANCED
SCIENCE NEWS**

www.advancedsciencenews.com

**ADVANCED
MATERIALS**

www.advmat.de

a nanocrystalline phase with a low stacking fault energy[15] can coexist with a MG phase.
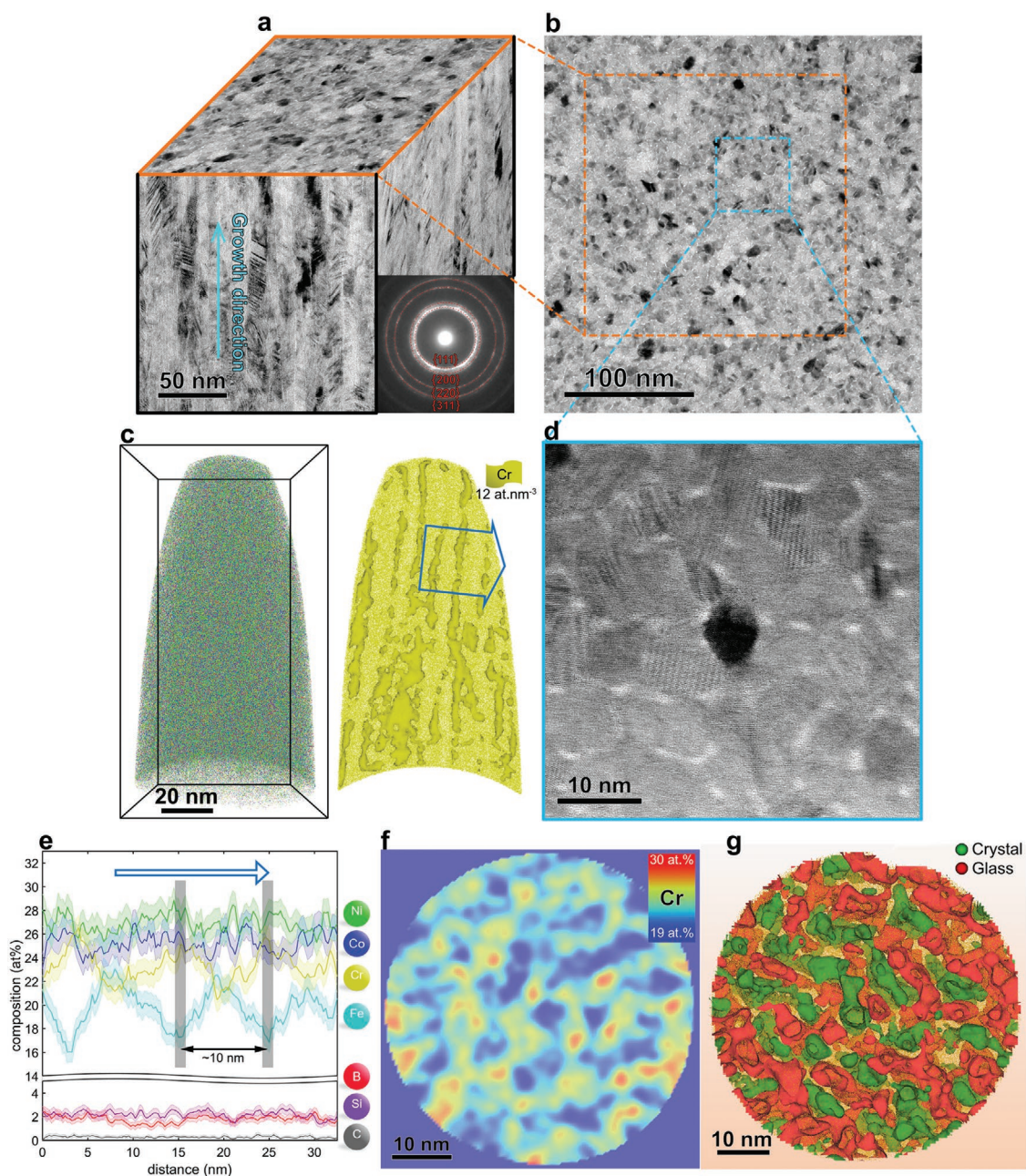
The crystal–glass high-entropy nanocomposite introduced here was obtained by doping a glass-forming Fe–Si–B system into a crystalline CrCoNi base alloy. These CrCoNi–Fe–Si–B nanocomposites were synthesized by magnetron co-sputtering of CrCoNi and $Fe_{78}Si_9B_{13}$ alloy targets with 99.9 at% purity (Experimental Section, Supporting Information). Through tuning the substrate-to-target distance differences,[16] alloys with varied compositions and structures were produced (Figure S1, Supporting Information). The composition of the crystal–glass high-entropy nanocomposite investigated in the following is 23.1 at% Cr, 20.7 at% Fe, 24.8 at% Co, 26.7 at% Ni, 1.7 at% B, 0.3 at% C, 0.6 at% O, and 2.1 at% Si, revealed by atom probe tomography (APT). The alloy grows in a nanocolumnar structure with ≈8 nm-wide face-centered cubic (fcc) phase with weak crystallographic texture (**Figure 1**a and inset). The amorphous phase with an average thickness of ≈1 nm is formed between these nanograins, as shown by the bright interface between them, revealed in the low-magnification transmission electron microscopy (TEM) image (Figure 1b) and annular bright-field scanning TEM (ABF-STEM) image (Figure 1d and Figure S2, Supporting Information). The detailed characterization methods are included in Experimental Section, Supporting Information. The amorphous phase does not cover all of the grain interfaces, but occupies most of the triple junctions. This topology may arise from the faster elemental diffusion along the triple junctions.[17] The amorphous phase is enriched in Cr, revealed by the APT analysis (Figure 1c). The compositional profile (Figure 1e) confirms that the crystalline and amorphous phases are enriched in Fe and Cr, respectively. B, C, O, and Si are as regular solutes distributed uniformly across the two phases. A 2D contour plot of the Cr concentration (Figure 1f) shows that Cr is enriched in the triple junctions, matching the results from the ABF-STEM analysis (Figure 1d). The grain boundary regions of the nanocrystalline reference CrCoNi alloy (without any amorphous phase) are also enriched in Cr (Figure S3, Supporting Information), driven by the Gibbs adsorption isotherm, as reported before for the case of Cr in CrCoNi-based alloys.[18] In the following, we discuss the glass-forming mechanism behind the amorphous phase in such a crystal–glass high-entropy nanocomposite. Fe–Co, Co–Ni, and Fe–Ni mixtures can each readily form single fcc solid solutions upon quenching over wide composition ranges,[19] indicating their high mutual miscibility. However, if Cr is introduced and its content exceeds 20%, complex intermetallic or other phases form as shown by the Fe–Cr, Co–Cr, and Ni–Cr phase diagrams.[19] According to metallic glass-forming theory, near-eutectic compositions enhance a material's glass-forming ability (GFA).[20] Also, B, C, O, and Si dopants can further enhance the GFA,[21] owing to their directional bond contribution. It is worth noting that the size of the amorphous phase regions (Figure 1g) in the present nanocomposite is below a critical value,[13,14] shifting it into a range where homogeneous plastic flow is observed in MGs. This means that the deformation behavior of the amorphous phase in the current material should be different from that of conventional monolithic MGs, as will be discussed below.

We further performed low-angle annular dark-field (LAADF)-STEM analysis to reveal the cross-sectional structure of the crystal–glass high-entropy nanocomposite (**Figure 2**). The nanotwins and stacking faults (SFs) are formed along the {111} habit plane, and assume a typical Kurdjumov–Sachs (K–S) relationship with the adjacent crystalline matrix, that is, $[1–10]_{twin}$ // $[–110]_\gamma$. Since the crystallographic texture in the columnar grains is very weak (inset in Figure 1a), the twins occur on all possible {111} <112> twinning systems without preference of a specific twin system. Figure 2a,b show two columnar grains with different twin orientations. The grains are mostly composed of high-density nanotwins with a spacing below 2 nm (Figure 2c,d). The average twin density is estimated to be 1.0×10^9 m^{-1}. Full dislocations are not detected in most lamellae, but SFs are frequently revealed. The high-density twins and SFs subdivide the ≈8 nm-wide grains into a sub-2 nm-thick twin/SF/matrix lamellar nanostructure. The nanotwin feature is not uncommon for metals that have low stacking fault energy and are produced by deposition,[22] but such high density of nanotwins is difficult to realize. The stacking fault energy of the CrFeCoNi HEA is known to be ≈27 mJ m^{-2},[15] which is sufficiently low to promote twin formation. The nonequilibrium state promoted by the high cooling rate of about 10^{10} K s^{-1} in sputter deposition[23] could be responsible for such a high-density nanotwin structure. Further, some of the nanotwins are higher-order multiple nanotwins (Figure 2b). The densely stacked twin boundary arrays are very effective barriers against dislocation motion,[22,24] providing substantial strength increase which is inversely proportional to the reduced dislocation mean free path. They also enhance the material's ductility as each nanotwin acts itself as an additional independent shear carrier and further provides an additional kinematic degree of freedom for dislocation movement inside the nanotwinned regions.[25]

The mechanical properties of the crystal–glass high-entropy nanocomposite have been probed by micro-compression tests. For comparison and reference, pure single-crystalline CrCoNi, nanocrystalline CrCoNi, and nanocrystalline CrCoNi–Fe–Si–B alloys without any amorphous phase have also been investigated under identical conditions. The detailed characterization methods are included in the Experimental Section (Supporting Information). The compressive engineering stress–strain curves in **Figure 3**a show that the nanocrystalline CrCoNi and CrCoNi–Fe–Si–B alloys have higher yield strength (3.3 and 3.8 GPa using the 0.2% strain criterion, respectively) than the single-crystalline CrCoNi (0.7 GPa). The nanocrystalline CrCoNi and CrCoNi–Fe–Si–B alloys have an average grain width of ≈20 nm and ≈15 nm, respectively. Both alloys contain columnar grains with a nanotwin structure (Figure S1, Supporting Information), which contribute to the higher strength via grain/twin boundary strengthening. The decrease of the flow stress, occurring during plastic deformation of the two alloys, is due to the abrupt formation and percolation of shear bands. These shear/slip bands are denoted by the red arrows in Figure 3c–e. In nanocrystalline materials, plastic deformation can also be accompanied by grain boundary (GB) motion (i.e., load-driven grain growth),[26] GB sliding or grain rotation, mechanisms which can also lead to strain softening. These mechanisms can result in frequent strain localization and restrict homogeneous plastic deformation, which are undesired effects often observed in nanocrystalline alloys. It is worth noting that the pure single-crystalline CrCoNi, nanocrystalline CrCoNi, and

**ADVANCED
SCIENCE NEWS**

www.advancedsciencenews.com

**ADVANCED
MATERIALS**

www.advmat.de

Figure 1. Structure and composition of the crystal–glass high-entropy nanocomposite. a) Typical bright-field plane-view and side-view TEM images. The inset shows a selected-area electron diffraction (SAED) pattern obtained from side-view TEM probing. The ring feature in the SAED pattern indicates that the nanocolumnar grains have weak crystallographic texture. An fcc structure is indexed, and the corresponding {111}, {200}, {220}, and {311} planes are highlighted by the dashed red rings. b) Low-magnification plane-view TEM image. c) 2 nm-thick slice (right part of (c)) from 3D reconstruction of an APT dataset (left part of (c)), showing that Cr is enriched at several locations at the grain–grain interfaces. The Cr enriched regions are highlighted by an iso-concentration surface in terms of a 12 at nm^{-3} Cr threshold value. d) Plane-view ABF-STEM image shows ≈1 nm-thick amorphous phase (brighter regions) appearing at triple points and along some grain boundaries. e) 1D compositional profile across the region indicated by the arrow in the right part of (c). The light shadows indicate statistical errors in terms of the standard deviations. f) 2D contour plot in terms of the Cr concentration of a 1 nm-thick plane-view slice from (c), showing the distribution of the Cr-enriched amorphous phase. g) Iso-concentration surfaces in terms of 22.7 at% Fe and 18.3 at% Fe threshold values, illustrating crystal and glass, respectively.

nanocrystalline CrCoNi–Fe–Si–B alloys can be compressed to 50% strain (gray, black and blue curves in Figure 3a), but this does not essentially reflect their true formability. These rather large apparent compressive strain values are partially caused by a compression instability,[27] i.e., by inhomogeneous plastic flow, which is due to shear/slip band percolation during pillar deformation (Figure 3c–e). What is important here is that the crystal–glass high-entropy nanocomposite displays the highest yield strength of 4.1 GPa among all reference materials probed, and also a large, homogeneous plastic strain above 45%, as

**ADVANCED
SCIENCE NEWS**

www.advancedsciencenews.com

**ADVANCED
MATERIALS**

www.advmat.de
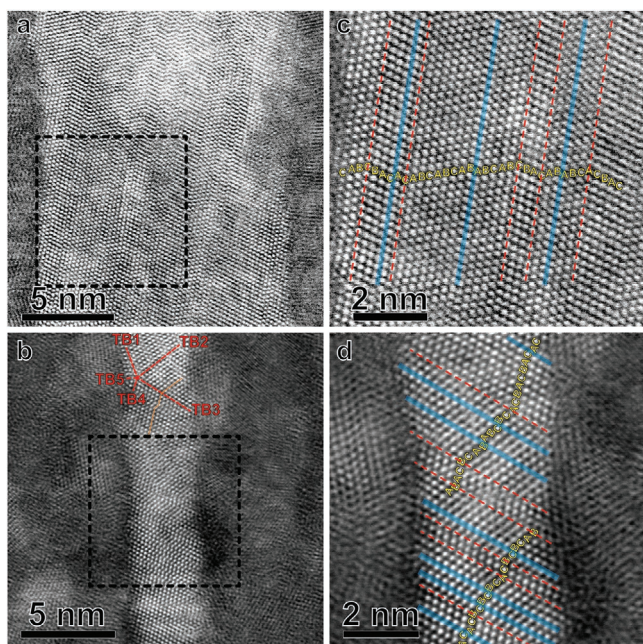
Figure 2. Crystalline structure of the nanograins in the as-prepared crystal–glass high-entropy nanocomposite. a) Cross-sectional LAADF-STEM image of a columnar grain with fcc structure that contains high-density nanotwins of 1.0×10^9 m^{-1}. b) Another columnar grain containing fivefold nanotwins. The five twin boundaries are marked with TB1, TB2, TB3, TB4, and TB5, respectively. The orange lines indicate the atom packing sequence. c,d) Higher magnification images of the dashed rectangle areas in (a) and (b), respectively, showing sub-2 nm-thick twin/SF/matrix lamellar structure. The atomic stacking sequence is labeled by "A," "B," and "C." The twin boundaries and SFs are indicated by dashed red and solid blue lines, respectively.

shown in Figure 3a,b. Pillar samples with four different diameters, that is, 380, 400, 500, and 1 µm, were tested. The yield strength of the samples in this size regime remains constant

(Figure S4, Supporting Information). Usually, the mechanical size effect associated with strength appears when the sample size becomes comparable to the correlation length of the defects that carry the plastic deformation,[28] that is, extremely small samples with low probability of containing defects or defect sources are usually stronger than those contain a mean field equivalent defect population.[29] In the current crystal–glass high-entropy nanocomposite, a 380 nm pillar diameter translates to more than 40 times the grain width (≈8 nm), which means that the mechanical size effect is negligible in this range. When calibrated by the shear modulus (G) and the shear strength (τ), G-to-τ ratio value is $G/\tau = 24$ for the current crystal–glass high-entropy nanocomposite. G is estimated using the equation $G = E/[2(1 + \nu)]$, with ν being the Poisson's ratio and E the Young's modulus, that is, $E = 124$ GPa, as obtained from nanoindentation. τ is calculated using $\tau = \sigma_y/2$,[10] where σ_y is the yield strength. This estimate shows that the observed G-to-τ ratio of the current crystal–glass high-entropy nanocomposite indeed approaches the theoretical strength[7] for this composition, already at the onset of yielding, due to the high stiffness of its crystal–glass nanostructure.[30,31] On the one hand, the thin amorphous phase in the interfacial regions between the grains increases the stress barrier for dislocation nucleation.[30,31] On the other hand, the strength of the nanotwinned crystalline phase increases with decreasing twin spacing, reaching a maximum value at a specific twin thickness (e.g., 15 nm for a 500 nm-grain-size nanotwinned Cu).[22] If the grain size is reduced, the maximum strength will be further improved by decreasing the twin thickness.[32] In the crystalline phase of the nanocomposite the grain width is ≈8 nm and the twin thickness is only ≈2 nm, yielding the highest possible twin boundary strengthening effect[32] in the crystalline phase. The amorphous phase surrounding the grains reduces the softening effect[32] of grain boundary–twin intersections. Conventional ultrastrong fcc alloys with such a high twin density (twin thickness < 2.8 nm) usually exhibit brittle fracture due to shear
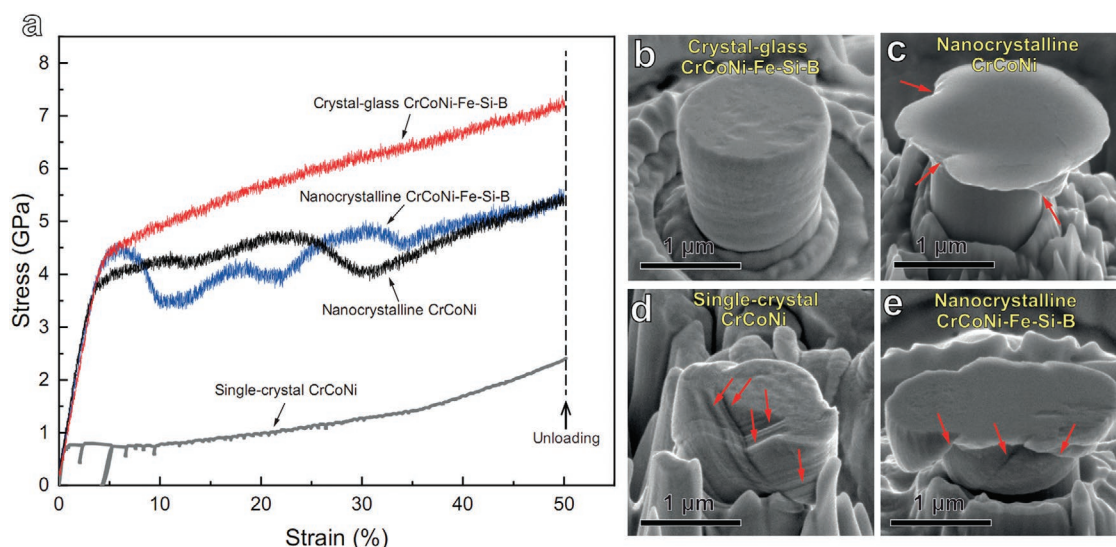
Figure 3. Mechanical properties of the crystal–glass high-entropy nanocomposite. a) Compressive engineering stress–strain curves of the crystal–glass CrCoNi–Fe–Si–B high-entropy nanocomposite, nanocrystalline CrCoNi–Fe–Si–B, nanocrystalline CrCoNi, and single-crystal CrCoNi pillar samples, each with the same diameter of 1 µm. b–e) SEM images of the same samples after compression to an identical engineering strain of 50%. Some of the shear bands in (c) and (e), and slip bands in (d) are indicated by red arrows.

ADVANCED
SCIENCE NEWS

www.advancedsciencenews.com

ADVANCED
MATERIALS

www.advmat.de

localization,[33] similar to the deformation behavior found here for the nanocrystalline CrCoNi-based reference alloys, Figure 3. However, the current crystal–glass high-entropy nanocomposite shows a large regime of homogeneous plastic deformation without any brittle fracture features. This finding shows that near theoretical strength values can be achieved together with high plastic formability when combining nanoscale MG regions with nanocrystals containing a high density of nanotwins.

APT and LAADF-STEM analyses were performed on the deformed pillars (**Figure 4**a) at a total engineering strain of ≈50% to investigate the underlying deformation mechanisms. Upon deformation, the nanocolumnar structure has—in the deformed pillar—transformed into globular units with a diameter of ≈8 nm (Figure 4b–f). This observation indicates that the nanocolumar grains have been cut and refined into smaller structure units, and no grain growth has occurred. In the transition region between the deformed pillar and the base material, the crystals have assumed a bent shape (Figure 4b–d) intermediate deformation zone. Near-atomic scale analysis was conducted by APT in a way that the tip was milled out with one end in the deformed pillar and the opposite one in the base material (Figure 4a) where the grains have maintained their straight columnar shape.

Interface features of the material in the reconstruction of the APT dataset have been highlighted in terms of a Cr iso-concentration surface (10 at nm^{-3}) to reveal the three deformation regimes, viz. the un-deformed base material, the bent transition region and the heavily deformed pillar (Figure 4b). The Cr is used here as a tracer to reveal these zones of different deformation, owing to its enrichment in the amorphous phase. In the deformed pillar, the Cr-enriched amorphous phase covers the globular grains (Figure 4b and Figure S5, Supporting Information) without occurrence of any shear banding feature, that is, showing instead a homogeneous plastic flow pattern. This behavior is a distinct feature of the current nanocomposite, because bulk MGs usually exhibit limited formability due to plastic instability caused by shear bands.[9] The excellent plastic compliance of the amorphous phase in the triple lines and grain boundary regions is due to its small size, exploiting the good intrinsic plastic deformation of MG at the nanoscale where shear bands remain confined.[13,14] When amorphous/crystalline nanolaminates are severely deformed, localized deformation may induce atomic-scale intermixing inside the shear bands.[34] Similarly, the compositions of the formerly Cr-enriched and depleted regions have become intermixed in the deformed pillar. The Cr concentration of the amorphous phase is gradually increased (more red-colored zones) in the intermediate transition region and assumes a maximum (highest intensity red color) in the deformed pillar, Figure 4c. The statistical concentration histograms of Cr, Fe, Co, and Ni are shown in the Figure S6, Supporting Information, which confirms the compositional changes in the amorphous and the crystalline phases. The results suggest that the dislocations generated in the crystalline phase drag Cr towards the crystal–glass interface and then further into the amorphous phase which absorbs the dislocations together with the dragged Cr.[34,35] Plastic flow of the amorphous phase is enabled through its nanoscale size,[13,14] and it becomes also a source for emitting fresh partial dislocations into the adjacent nanograins.[31] The partial dislocations

move inside the nanograins and interact with the pre-existing nanotwins and SFs, inducing twin boundary migration, leading to the observed de-twinning mechanism (Figure 4e). Furthermore, the amorphous phase which undergoes plastic flow[13,14] has near ideal strength[14] which prevents shear band formation. This behavior effectively impedes instable deformation and prevents load-driven grain growth. The dislocations flow through the entire nanograins, causing their gradual subdivision. This mechanism and the associated increase of the interface density between the amorphous phase and the grains upon plastic deformation create additional obstacles for dislocation motion, providing additional strain hardening. On the other hand, the twin density in the deformed grains gradually decreases (Figure 4f) due to mechanically-driven de-twinning. The average twin density is estimated to decrease from $(1.0 \pm 0.2) \times 10^9$ m^{-1} to $(5 \pm 1) \times 10^8$ m^{-1} after 50% deformation. De-twinning processes usually result in strain softening.[33] However, in the crystal–glass high-entropy nanocomposite, strain hardening from the newly formed amorphous phase/grain interfaces compensates the softening associated with the de-twinning. The dissociation of partial dislocations interacting with twin boundaries mitigates stress concentration effects which would otherwise occur due to dislocation pile-up. Dislocation dissociation thus reduces these stress peaks and enhances ductility.[25] One has to note that it is difficult to directly locate partial dislocations inside of the deformed nanograins (Figure 4f). This is due to the fact that practically no obstacles exist inside the grain interiors so that the dislocations instantaneously penetrate the crystal and annihilate at the opposite interface during deformation. In fact, nano-sized amorphous phase regions have been observed as effective sinks for dislocations.[31,34] The continuous generation, movement, and annihilation of the partial dislocations does not lead to formation of any pile-up configurations (Figure 4g), thus promoting homogenous and compatible plastic deformation of the crystal–glass nanocomposite.

In summary, a novel crystal–glass high-entropy nanocomposite was developed by combining a nanocrystalline HEA phase with a nanoscale amorphous MG phase in one alloy concept, taking advantages of both, the low stacking fault energy of the HEA phase and the compliant nature of the MG phase at the nanoscale. The concept was realized by doping the glass-forming elements B and Si into a Cr–Fe–Co–Ni high-entropy base alloy system. The nano-sized amorphous phase regions wrapping the nanocolumnar grains containing high-density nanotwins leads to a material with a high yield strength of 4.1 GPa (here probed under compressive load). The high strength which approaches the theoretical shear strength limit results from a synergistic strengthening hierarchy including the duplex crystal–glass structure, the interface-dislocation interactions, the nanoscopic size scales of the crystalline and glassy building units and the high-density nanotwins in the crystalline grains. The plastic flow of the amorphous phase, the partial dislocation flow and the deformation-induced refinement of the nanograins during deformation result in a homogeneous plastic deformation above 45%. The findings illustrate the advantages associated with the introduction of a new material class which merges concepts from HEAs, MGs, and nanoscience. It is shown that this new alloy- and nanostructure design approach does not only enable ductile materials with near theoretical strength but can be tuned
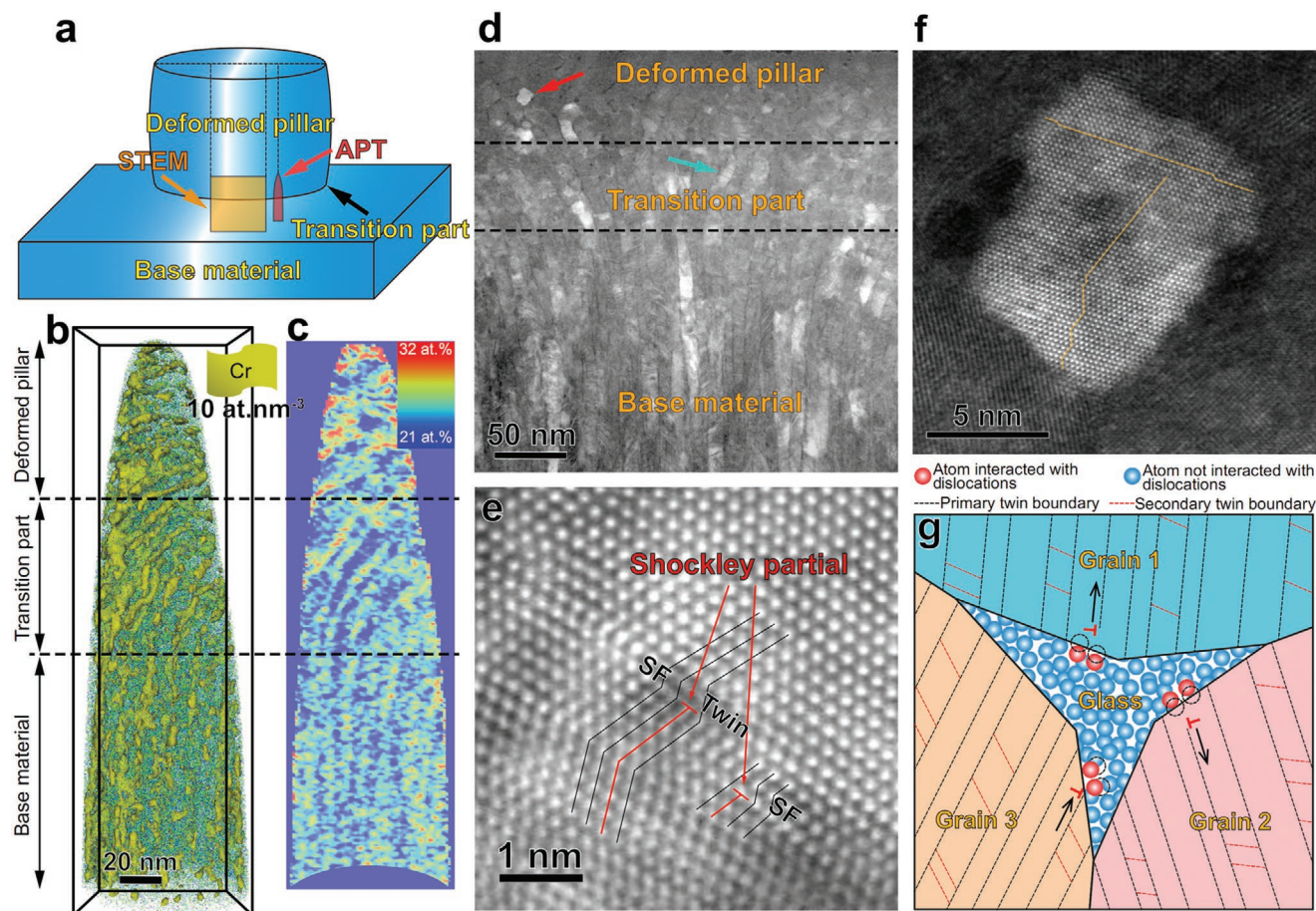
Figure 4. Plastic deformation mechanism of the crystal–glass high-entropy nanocomposite. a) Schematic indicating where APT and STEM probing were conducted. b) 3D reconstruction of an APT dataset where some of the interfacial features are highlighted and revealed in terms of an iso-concentration surface of Cr (10 at nm^{-3}), showing three zones, namely, the heavily strained "deformed pillar", the "transition part" (with bent columnar grains) and the "base material" (with the straight columnar grains) regions. c) 2D contour plot in terms of the Cr concentration of a 2 nm-thick slice from (b), showing Cr enriching in the "deformed pillar". d) Cross-sectional LAADF-STEM image of a deformed pillar which has undergone ≈50% total plastic engineering strain, together with the transition region and base material. The thickness of the transition region is about 80 nm, indicated by the dashed lines. The thickness is similar to the same region that was in the APT dataset identified in terms of composition features in (b). e) Enlarged cross-sectional LAADF-STEM image of a deformed nanograin in the transition region, indicated by the blue arrow in (d), showing twin boundary migration through the motion of Shockley partial dislocations. The black and red lines indicate the atom packing sequence. f) Enlarged cross-sectional LAADF-STEM image of a deformed nanograin in the deformed pillar, indicated by the red arrow in (d). The twin density of the nanograins has decreased to 5×10^{8} m^{-1} after deformation. The orange lines indicate the atom packing sequence. g) Illustration of the structure evolution during plastic deformation. Partial dislocations ("⊥") can be generated on the glass–grain (1 and 2) interfaces and then interact with nanotwins and SFs in the nanograins, inducing de-twinning. Partial dislocations ("⊥") can move inside the grain (3) and then be absorbed in the glass–grain interface (dislocation annihilation). The red and blue spheres represent atoms that interact more or less with the dislocations, respectively. The dashed circles represent the original positions of the atoms that interacted with dislocations. The dashed black and red lines represent the primary and secondary twin boundaries, respectively. The black arrows denote the motion directions of the dislocations.

to also feature further interesting properties such as functional soft magnetism (Figure S7, Supporting Information) and good thermal stability (Figure S8, Supporting Information), for instance for applications in mechanically high loaded micro-electromechanical systems and flexible devices.

Supporting Information

Supporting Information is available from the Wiley Online Library or from the author.

Conflict of Interest

The authors declare no conflict of interest.

[1] Z. Lei, X. Liu, Y. Wu, H. Wang, S. Jiang, S. Wang, X. Hui, Y. Wu, B. Gault, P. Kontis, *Nature* **2018**, *563*, 546.

[2] Z. Li, K. G. Pradeep, Y. Deng, D. Raabe, C. C. Tasan, *Nature* **2016**, *534*, 227.

[3] a) J. W. Yeh, S. K. Chen, S. J. Lin, J. Y. Gan, T. S. Chin, T. T. Shun, C. H. Tsau, S. Y. Chang, *Adv. Eng. Mater.* **2004**, *6*, 299; b) B. Cantor, I. Chang, P. Knight, A. Vincent, *Mater. Sci. Eng., A* **2004**, *375*, 213.

[4] E. P. George, D. Raabe, R. O. Ritchie, *Nat. Rev. Mater.* **2019**, *4*, 515.

[5] a) W. Lu, C. H. Liebscher, G. Dehm, D. Raabe, Z. Li, *Adv. Mater.* **2018**, *30*, 1804727; b) S. S. Sohn, A. K. da Silva, Y. Ikeda, F. Körmann, W. Lu, W. S. Choi, B. Gault, D. Ponge, J. Neugebauer, D. Raabe, *Adv. Mater.* **2019**, *31*, 1807142; c) H. Huang, Y. Wu, J. He, H. Wang, X. Liu, K. An, W. Wu, Z. Lu, *Adv. Mater.* **2017**, *29*, 1701678.

[6] Y. Zhang, T. T. Zuo, Z. Tang, M. C. Gao, K. A. Dahmen, P. K. Liaw, Z. P. Lu, *Prog. Mater. Sci.* **2014**, *61*, 1.

[7] A. Kelly, N. H. Macmillan, *Strong Solids*, Oxford University Press, Oxford, UK **1986**.

[8] W. K. Jun, R. Willens, P. Duwez, *Nature* **1960**, *187*, 869.

[9] A. L. Greer, *Science* **1995**, *267*, 1947.

[10] W. Johnson, K. Samwer, *Phys. Rev. Lett.* **2005**, *95*, 195501.

[11] a) J. Ding, S. Patinet, M. L. Falk, Y. Cheng, E. Ma, *Proc. Natl. Acad. Sci. USA* **2014**, *111*, 14052; b) J. Brechtl, H. Wang, N. Kumar, T. Yang, Y.-R. Lin, H. Bei, J. Neufeind, W. Dmowski, S. J. Zinkle, *J. Nucl. Mater.* **2019**, *526*, 151771.

[12] W. Li, H. Bei, Y. Tong, W. Dmowski, Y. Gao, *Appl. Phys. Lett.* **2013**, *103*, 171910.

[13] H. Guo, P. Yan, Y. Wang, J. Tan, Z. Zhang, M. Sui, E. Ma, *Nat. Mater.* **2007**, *6*, 735.

[14] D. Jang, J. R. Greer, *Nat. Mater.* **2010**, *9*, 215.

[15] S. Liu, Y. Wu, H. Wang, J. He, J. Liu, C. Chen, X. Liu, H. Wang, Z. Lu, *Intermetallics* **2018**, *93*, 269.

[16] M.-X. Li, S.-F. Zhao, Z. Lu, A. Hirata, P. Wen, H.-Y. Bai, M. Chen, J. Schroers, Y. Liu, W.-H. Wang, *Nature* **2019**, *569*, 99.

[17] M. R. Chellali, Z. Balogh, H. Bouchikhaoui, R. Schlesiger, P. Stender, L. Zheng, G. Schmitz, *Nano Lett.* **2012**, *12*, 3448.

[18] L. Li, Z. Li, A. K. da Silva, Z. Peng, H. Zhao, B. Gault, D. Raabe, *Acta Mater.* **2019**, *178*, 1.

[19] Computational Thermodynamics, http://www.calphad.com (accessed: January 2020).

[20] Z. Lu, H. Tan, S. Ng, Y. Li, *Scr. Mater.* **2000**, *42*, 667.

[21] a) S. Pang, T. Zhang, K. Asami, A. Inoue, *Acta Mater.* **2002**, *50*, 489; b) H. Li, J. Gao, Z. Jiao, Y. Wu, Z. Lu, *Appl. Phys. Lett.* **2009**, *95*, 161905.

[22] L. Lu, X. Chen, X. Huang, K. Lu, *Science* **2009**, *323*, 607.

[23] P. Bordeenithikasem, J. Liu, S. A. Kube, Y. Li, T. Ma, B. E. Scanley, C. C. Broadbridge, J. J. Vlassak, J. P. Singer, J. Schroers, *Sci. Rep.* **2017**, *7*, 7155.

[24] I. Gutierrez-Urrutia, D. Raabe, *Acta Mater.* **2011**, *59*, 6449.

[25] Y. Wei, Y. Li, L. Zhu, Y. Liu, X. Lei, G. Wang, Y. Wu, Z. Mi, J. Liu, H. Wang, *Nat. Commun.* **2014**, *5*, 3580.

[26] T. Fang, W. Li, N. Tao, K. Lu, *Science* **2011**, *331*, 1587.

[27] G. Dehm, B. N. Jaya, R. Raghavan, C. Kirchlechner, *Acta Mater.* **2018**, *142*, 248.

[28] M. D. Uchic, D. M. Dimiduk, J. N. Florando, W. D. Nix, *Science* **2004**, *305*, 986.

[29] S. Shim, H. Bei, E. P. George, G. M. Pharr, *Scr. Mater.* **2008**, *59*, 1095.

[30] G. Wu, K.-C. Chan, L. Zhu, L. Sun, J. Lu, *Nature* **2017**, *545*, 80.

[31] G. Wu, C. Liu, L. Sun, Q. Wang, B. Sun, B. Han, J.-J. Kai, J. Luan, C. T. Liu, K. Cao, Y. Lu, L. Cheng, J. Lu, *Nat. Commun.* **2019**, *10*, 5099.

[32] X. Li, Y. Wei, L. Lu, K. Lu, H. Gao, *Nature* **2010**, *464*, 877.

[33] J. Wang, F. Sansoz, J. Huang, Y. Liu, S. Sun, Z. Zhang, S. X. Mao, *Nat. Commun.* **2013**, *4*, 1742.

[34] W. Guo, E. A. Jägle, P.-P. Choi, J. Yao, A. Kostka, J. M. Schneider, D. Raabe, *Phys. Rev. Lett.* **2014**, *113*, 035501.

[35] M. Kuzmina, M. Herbig, D. Ponge, S. Sandlöbes, D. Raabe, *Science* **2015**, *349*, 1080.